Tomographic Reconstruction with Real-time *a priori* Acquisition

Muhammad Wishal Khan*
m.w.khan@greenwich.ac.uk
School of Computing & Mathematical Sciences
University of Greenwich
London, United Kingdom

Hooman Oroojeni
h.oroojeni@greenwich.ac.uk
School of Computing & Mathematical Sciences
University of Greenwich
London, United Kingdom

Bal Sanghera
bal.sanghera@nhs.net
Barts Health NHS Trust
London, United Kingdom

Tim Blackwell
t.blackwell@gold.ac.uk
Department of Computing
Goldsmiths, University of London
London, United Kingdom

Mohammad Majid al-Rifaie
m.alrifaie@greenwich.ac.uk
Computing & Mathematical Sciences
University of Greenwich
London, United Kingdom

Abstract

An *a priori* construction technique is proposed, utilizing a minimal swarm optimizer to achieve enhanced reconstruction accuracy. Central to the method is the incorporation of *a priori* information, constructed dynamically without prior knowledge of material properties, positions, or structural details. Instead, this *a priori* information is derived directly from sinogram projections for each defined angle in the set. A novel dynamic masking strategy leverages these sinogram-derived values to identify certain entries, generating *a priori* data structure that removes regions in the reconstructed image corresponding to zero sinogram values, thereby achieving theoretical dimensionality reduction. This approach effectively eliminates noise and artifacts, resulting in significantly lower reconstruction and reproduction errors.

CCS Concepts

• **Computing methodologies** → **Image processing**; • **Theory of computation** → **Bio-inspired optimization**.

Keywords

Swarm intelligence, tomographic reconstruction, *a priori*, denoising, regularization

1 Introduction

Tomographic reconstruction is a computational technique that involves reconstructing an image or object from its projection data, typically acquired using imaging modalities such as computed tomography (CT) or X-ray imaging. These projections represent integrals of the internal structures of the object along defined paths, and the reconstruction process aims to reverse this transformation to generate a detailed representation of the internal composition of the object.

In the context of tomographic reconstruction, the challenge of few-view reconstruction arises when the number of projection angles is severely limited due to constraints such as reduced acquisition time, radiation dose minimization, or hardware limitations. Such under-sampled data leads to an ill-posed reconstruction problem which is under-determined, characterized by significant artifacts, loss of detail, and reduced reconstruction accuracy. The available information is insufficient to uniquely and accurately determine the object, and as a result, noise is introduced and propagated throughout the reconstruction process which results in distortion and corruption of the reconstruction image.

Conventional reconstruction methods, such as filtered backprojection (FBP) [42], are computationally efficient, requiring only one iteration [29], but are generally unsuitable for scenarios with limited projection views [29]. Despite its efficiency, FBP often amplifies noise and introduces streak artifacts, particularly in reconstructions with sparse or noisy projection data [29]. Recent advancements in computational power have facilitated iterative methods like Algebraic Reconstruction Techniques (ART) [27], which rely on Kaczmarz's method [31] to address the challenges of few-view imaging. ART sequentially updates the solution as an iterative method by projecting back individual ray sums, making it effective for sparse-view problems, however, this methodology is prone to introducing artifacts, such as noise amplification and overfitting, particularly in cases with sparse data.

Simultaneous Iterative Reconstruction Technique (SIRT) [25] is particularly robust in handling incomplete data and demonstrates resilience to noise, making it suitable for sparse-view scenarios. However, while SIRT effectively reduces certain types of noise, it can still exhibit residual low-frequency noise patterns in the reconstructed images, especially when the initial guess is poorly chosen [25]. On the other hand, Simultaneous Algebraic Reconstruction Technique (SART) [12] is known for its fast convergence and ability to produce high-quality images. Despite this, SART is prone to streaking artifacts and noise propagation, particularly in cases of incomplete projection data [46]. Additionally, both methods come with significant computational demands [38], further limiting their scalability for real-time applications or large-scale reconstructions.

GECCO '25, July 14–18, 2025, Málaga, Spain

Deep learning contributes solutions to challenges like noise reduction, artifact suppression, and enhanced image quality in limited-data scenarios. Methods such as multi-layer clustering-based residual sparsifying transform [19], hierarchical decomposition of domain transforms [24], and residual neural networks for monochromatic imaging [20] exemplify the advancements. These approaches leverage advanced neural architectures, such as U-Net [30], CycleGAN [18], and model-based deep learning [47], to integrate prior knowledge, refine reconstructions, and address ill-posed inverse problems. Despite notable successes, including reduced errors and improved metrics, several challenges persist, such as dataset dependency, high computational costs, and limited generalizability to diverse clinical settings.

Swarm intelligence is a computational methodology which is rooted in the self-organizing behavior of decentralized systems where it has shown significant potential in addressing the challenges of few-view tomographic reconstruction (TR). Algorithms inspired by biological systems, such as Particle Swarm Optimization (PSO) [34], Ant Colony Optimization (ACO) [21], and Artificial Bee Colony (ABC) [32], effectively navigate non-convex, high-dimensional search spaces, making them well-suited for the ill-posed nature of limited-data TR [22, 23, 34]. Herman and Kuba [28] applied PSO to handle data scarcity in discrete TR, ensuring particle convergence within defined limits while demonstrating its feasibility on binary matrices. Similarly, Qureshi et al. [41] addressed few-view reconstruction in low-dose CT by optimizing cost functions such as RMSLE, enabling Simulated Annealing (SA) to reduce artifacts and improve image quality, outperforming Filtered Back Projection (FBP) and Algebraic Reconstruction Technique (ART). Mishra [36] proposed a Hybrid Multiagent-Based Adaptive Genetic Algorithm (HMAGA) for limited-view tomography, leveraging adaptive rates, oppositional learning, and simulated annealing to enhance convergence. Polar Bear Optimization (PBO), which is designed for incomplete data scenarios, has utilized parallelized computations to expedite convergence while improving reconstruction accuracy in few-view contexts [40]. Additionally, heuristic methods like ABC outperformed traditional approaches in stability and convergence speed, effectively adapting to sparse projections and enhancing reconstruction precision [39].

This paper reports on a comparative analysis of a standard version of a minimlaist swarm optimiser-dispervise flies optimization (DFO), and DFO with a priori-informed dimensionality reduction (DFO-DR), alongside classical reconstruction algorithms such as ART, FBP, and SIRT. The key differentiator for DFO-DR lies in its incorporation of angular *a priori*, which systematically masks non-contributing regions of the reconstruction domain. This dimensionality reduction process significantly reduces the number of pixels requiring reconstruction, thereby focusing reconstructions on valid regions, thereby eliminating peripheral noise and artifacts.

When compared to standard DFO, DFO-DR consistently outperforms in benchmark experiments. The dimensionality reduction enabled by the *a priori* map not only enhances computational efficiency but also reduces noise propagation, resulting in higher-quality reconstructions. Visual comparisons further corroborate these findings, with DFO-DR reconstructions exhibiting significantly less noise and sharper delineation of object boundaries. These results underscore the transformative impact of integrating angular *a priori* with swarm optimization techniques, enabling focused and efficient reconstruction while achieving superior image quality relative to both standard DFO and classical reconstruction methods.

2 Dispersive Flies Optimization

Dispersive Flies Optimization (DFO) is a minimal implementation of Particle Swarm Optimization (PSO) without memory [2]. Positional vector updates are relative to present position and not historical position. The algorithm functions by determining the best global position g^{t+1} and the best neighboring positions n_i^{t+1} in a ring topology. Unlike standard PSO, DFO deploys a probabilistic jump mechanism [16] as part of the process to update each position. The exploration and exploitation behavior of the algorithm is investigated in [3].

The update follows a process where, for each particle i, if a randomly drawn value $u \sim U(0,1)$ is less than a predefined jump probability Δ, the positional component x_{id}^{t+1} is redrawn from a uniform distribution along the search space axis d, denoted as $U(X_d)$:

$$x_{id}^{t+1} \sim U(X_d), \quad \text{if } u \sim U(0,1) < \Delta \tag{1}$$

Otherwise, the position update is guided by the local best neighbor, adjusted by a weighted perturbation term involving the global best position:

$$x_{id}^{t+1} = n_{id}^{t+1} + \phi u_1 (g_d^{t+1} - x_{id}^t) \tag{2}$$

where $u_1 \sim U(0,1)$ and ϕ is a scaling factor typically constrained to the range $[0, \sqrt{3}]$ based on convergence analysis of stochastic difference equations [16]. The algorithm integrates both global and local search strategies, with two tunable parameters: N (swarm size) and Δ (jump probability). In prior studies, ϕ has been consistently set to 1. The algorithm has been applied to a wide range of problems in computer vision, aesthetics measurement and art, optimizing food processes, placement of unmanned aerial vehicles, electronics, data science and neuroevolution [1, 4, 9–11, 13–15, 37].

2.1 DFO and Few-View Tomographic Reconstruction

Researchers who have applied DFO to the reconstruction problem, in their work [6], proposed a high diversity swarm optimizer to binary tomographic reconstruction under few-view scenarios DFOMAX.

In subsequent work [5], DFO was also compared with conventional and swarm intelligence algorithms on five reconstruction phantoms, including the 2-dimensional clinically feasible Shepp-Logan phantom. The experiments incorporated clamping to confine particle movements within the search space boundaries. Pre-optimization comparisons showed that DFO underperformed in one of the metrics, reconstruction error, e_1 (see Eq. 5 which examines the phantom's projection data against those of the reconstructed images) compared to ART, SART, and SIRT, but excelled in another metric, reproduction error, e_2 (see Eq. 6 which measures the reconstructed image's similarity to the original phantom) against LPSO and Differential Evolution (DE). Hyperparameter tuning is

performed and experiments are run again using the optimized version (DFO-TR) which achieved the lowest $e2$ much improved $e1$, with the study suggesting hybridization of DFO with conventional methods for further improvements.

Further works include [7] where a search space expansion process is proposed via enlargement of the search space in a series of increasing sizes as a measure of mitigating premature convergence. The swarm optimizer searches in a series of progressively larger subspaces until the final subspace is identical to the full search space. Experiments are conducted with the same hyperparameter and experimental settings from [5]. The proposed methodology was successful in eliminating salt-and-pepper noise where statistical tests confirmed that increasing the number of search space expansions up to 50 boxes significantly reduces reproduction error, with diminishing returns beyond 50 boxes. Comparisons to classical methods like ART, FBP, SART and SIRT showed DFO-50 achieved the lowest median reproduction error for all projections and outperformed SIRT in reproduction quality, despite SIRT producing the lowest reconstruction error. The combination of boxing and clamping strategies effectively eliminated noise, resulting in artifact-free reconstructions. DFO-50 demonstrated superior performance over other population-based algorithms, such as PSO and DE.

Further refinement to the search space expansion methodology is performed via total variation regularization by [8] to eliminate salt-and-pepper noise which is reported to increase the fidelity of reconstructed image in comparison to the original phantom. The experimental results found that the e_1 error increased, however, this was complemented by a decrease in the e_2 error thereby successfully increasing the reproduction quality.

2.2 Use of *a priori* information in reconstruction

In the context of tomographic reconstruction, *a priori* refers to predefined information or assumptions about the object being reconstructed, which are integrated into the reconstruction algorithm to provide additional constraints. *a priori* can take various forms depending on the application and the nature of the object. Common examples include assumptions about the smoothness of the reconstructed image, sparsity of certain features, uniformity within specific regions, or known boundaries of materials or structures within the object [17]. Various types of *a priori* are employed to enhance image quality and address challenges posed by limited or noisy data. Geometric *a priori* incorporate known structural information, such as shapes or boundaries, to improve the accuracy of reconstruction algorithms in representing an object's geometry, particularly in constrained scenarios [35]. Statistical *a priori* leverage probabilistic models, including assumptions about noise distributions or image correlations, to guide the reconstruction process by integrating prior statistical knowledge [26]. Sparsity *a priori* assumes that the target image has a sparse representation in specific domains, such as wavelets or gradients, enabling high-quality image recovery by promoting solutions with minimal non-zero coefficients, thereby mitigating noise and artifacts [43]. Additionally, learned *a priori* rely on machine learning models trained on large datasets to capture intricate patterns and structures, allowing for more nuanced and data-driven reconstructions [44]. These *a priori* collectively form a robust framework for improving reconstruction fidelity across diverse tomographic applications.

3 Problem Statement

Parallel rays are used to model incident beams, with each ray striking the center of a detector or projection bin. The imaging process is represented by a projection matrix $A \in \mathbb{R}_{\geq 0}^{m \times n}$, where m denotes the total number of rays collected, calculated as the product of the number of rays per projection angle and the number of projection angles, and n represents the number of pixels in the reconstructed image. Given a vector of detector values $b \in \mathbb{R}^m$, the reconstruction problem, whether continuous or discrete, can be expressed as:

$$\text{find } x \begin{cases} \in \mathbb{R}^n \\ \in \{0, 1, \ldots, k-1\}^n, k > 1 \end{cases} \quad \text{such that } Ax = b \tag{3}$$

The binary problem is $k = 2$ i.e. with $x \in \{0, 1\}^n$. Since the equation $Ax = b$ is, in general, underdetermined, it cannot be inverted. Instead an approximate solution y must be obtained (e.g. by filtered back projection, or by algebraic reconstruction). This trial solution is forward projected according to the measurement model:

$$Ay = c \tag{4}$$

with an associated reconstruction error

$$e_1(y) = \|b - Ay\|_2^2 \tag{5}$$

An iterative approach generates a sequence of candidate solutions, denoted as $y^{(k)}, k = 1, 2, \ldots$, with each iteration producing solutions that progressively reduce the associated error.

In the case of a binary reconstruction problem, $k = 2$, meaning $x \in 0, 1^n$. Since the equation $Ax = b$ is typically underdetermined, it cannot be directly inverted. Therefore, an approximate solution y must be determined using methods such as filtered back-projection or algebraic reconstruction. This approximate solution is then forward projected according to the measurement model:

$$e_2 = \|y - x^*\|_1 \tag{6}$$

A zero value of e_1 indicates that the equation $Ay = b$ has been satisfied; however, this does not ensure that the reconstructed image faithfully represents the original phantom. The reproduction error e_2 serves as an additional metric, where a value of zero signifies that the reconstructed image is an exact replica of the original, thereby it is representative of the image reconstruction quality.

Previous works incorporating *a priori* have mainly focused on the integration of known information such as the location, shape, or material properties of the object being reconstructed. These approaches leverage predefined geometrical or structural information to constrain the solution space, often resulting in improved accuracy and reduced noise or artifacts in the reconstructed images. For instance, *a priori* such as boundary contours, known symmetries, or sparsity assumptions have been utilized to enhance reconstructions in scenarios with limited or noisy projection data. However, these methods typically rely on prior knowledge obtained through external measurements, additional imaging modalities, or user-defined inputs, which may not always be available or practical in real-world applications.

Tomographic reconstruction in sparse or few-view scenarios becomes significantly more challenging when no prior geometric information or material properties of the object are available. In such cases, reconstruction algorithms must operate in a blind setting, relying solely on the projection data for guidance. This lack of external information exacerbates the ill-posed nature of the inverse problem, as the limited and incomplete sinogram data provide insufficient constraints for accurate reconstruction.

This problem becomes even more complex when dealing with diverse projection angles, where the relationship between detector values and intersected regions in the reconstruction space must be inferred entirely from the sinogram. Developing a framework capable of constructing these *a priori* maps in real-time is critical for enabling efficient and high-quality tomographic reconstruction under blind conditions, where no *a priori* knowledge is available.

3.1 Challenges with Constructing Real-Time *a priori* Information

Constructing an *a priori* map from unknown or partially available information, such as sinogram data, is a challenging task due to the inherent ill-posedness and under-determined nature of the tomographic reconstruction problem. Unlike scenarios where prior knowledge is explicitly available – such as known material properties, geometry, boundaries, or structural details – deriving *a priori* from limited or noisy sinogram data requires the extraction of meaningful patterns and features directly from the projections. This process is complicated by the fact that sinograms often contain incomplete or corrupted information, especially in few-view or low-dose scenarios, where the data is insufficient to uniquely determine the underlying image [17].

Furthermore, sinogram data represents integrals along defined paths rather than direct spatial information, making it non-trivial to infer localized image features or structural properties. Any attempt to construct *a priori* must therefore involve sophisticated techniques to analyze and transform this projection data into constraints or assumptions that can guide the reconstruction process. Additionally, noise and inconsistencies in the sinogram further complicate the task, as these factors can propagate into the derived *a priori*, leading to inaccuracies or biases in the reconstruction [33].

3.2 Projection Geometry

The experiments reported in this work use the ASTRA Toolbox [45] which supports two key projection geometries: parallel beam and fan beam. In parallel beam projection, X-rays travel along parallel paths, ensuring uniform sampling and simplifying reconstruction, making it ideal for scenarios requiring consistent data across all angles. Fan beam projection, on the other hand, models X-rays diverging from a single source to a curved detector array, capturing localized details with higher resolution near the source. In the experiments reported in this work, the projection mechanism employed is the parallel beam projection. In parallel beam geometry, the projection at angle $\boldsymbol{\theta}$ is computed as the line integral of the object $f(x, y)$ along straight lines parallel to the detector array. The projection can be expressed mathematically using the Radon Transform:

$$P_\theta(s) = \int_{-\infty}^{\infty} f(s\cos\theta - t\sin\theta, s\sin\theta + t\cos\theta)dt \tag{7}$$

where $P_\theta(s)$ is the projection value at angle θ and position s along the detector; $f(x, y)$ represents the object being imaged; s and t are coordinates along the rotated axes determined by θ.

4 Real-Time *a priori* Construction

The focus of this work is to build on the existing research and to optimize the performance of swarm-driven tomographic reconstruction algorithm via dimensionality reduction of valid reconstruction regions. This is achieved via the construction of a real-time *a priori* map which is built from the sinogram projection values and incorporation of this as a masking mechanism to ignore regions not contributing to the sinogram values, thereby achieving simultaneous noise and artifact removal from the corresponding regions.

The prior in this implementation is defined as a two-dimensional *a priori* map which is responsible to keep track of the pixel positions and corresponding *a priori* `True`/`False` values. Each entry in the map corresponds to a specific pixel in the reconstruction grid, with a `True` value indicating that the pixel is valid and contributes to the reconstruction, while a `False` value signifies that the pixel should be masked due to insufficient or zero contribution from the projection's sinograms data.

Figure 1 shows the *a priori* map creation when different numbers of projections from several angles are used. The figure on the right is the original phantom whereas the 5 corresponding figures represent the *a priori* map for 1 angle (0° and 90° separately), 2 angles (0° and 90° together), 3 angles (0°, 45° and 90°) and 6 angles corresponding to the projection angles in the toolbox (0°, 30°, 60°, 90°, 120°, 150°).

4.1 Dimensionality Reduction

Dimensionality reduction in the context of tomographic reconstruction refers to the removal of unused or irrelevant regions in the data, effectively reducing the problem size and improving computational efficiency. This process focuses on eliminating areas that do not contribute meaningful information to the reconstruction, thereby simplifying the problem without affecting the quality of the reconstructed image. By excluding these unused regions, the reconstruction pipeline not only reduces the computational load but also mitigates the propagation of noise and artifacts from irrelevant areas. Another work related to low-dose computed tomography [33] demonstrated a similar approach where sinogram denoising techniques suppressed noise while retaining critical features, implicitly focusing only on the relevant regions of the data. Incorporating dimensionality reduction by removing unused regions ensures faster processing times and enhanced accuracy, particularly in scenarios where the data is sparse or affected by noise.

The reconstruction image is represented as a grid, corresponding to the total number of pixels in the image (i.e. width × height) which reflects the number of adjustable values to be optimized during the reconstruction process. The objective of dimensionality reduction is to restrict the reconstructable region to focus exclusively on the object(s) of interest, thereby reducing the range of updatable pixels. This targeted approach is designed to lower computational requirements and processing time while simultaneously

Figure 1: Sample phantom and corresponding *a priori* maps for increasing angular *a priori* masking. As the number of angular *a priori* increases, the final reconstructable region follows the original shape of the phantom more closely.

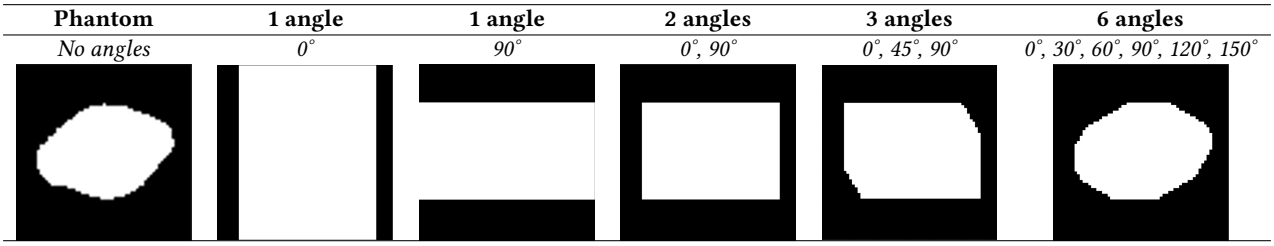

suppressing salt-and-pepper noise, particularly in the peripheral empty regions.

	Phantom 1	Phantom 2	Phantom 3	Phantom 4	Phantom 5
No *a priori*	4096 (100%)	4096 (100%)	4096 (100%)	4096 (100%)	4096 (100%)
1 Angle	3200 (78.12%)	3328 (81.25%)	1600 (39.06%)	3904 (95.31%)	2560 (62.5%)
2 Angles	1750 (42.72%)	2548 (62.21%)	825 (20.14%)	3599 (87.87%)	2160 (52.73%)
3 Angles	1673 (40.84%)	2500 (61.04%)	570 (13.92%)	3276 (79.98%)	2004 (48.93%)
6 Angles	1349 (32.93%)	2314 (56.49%)	367 (8.86%)	2959 (72.24%)	1784 (43.55%)

Table 1: Number of pixels for phantoms 1 to 5 after *a priori* map application. The search space is decreased as non-contributing pixels are removed.

Table 1 shows the dimension of the valid reconstruction region under different *a priori* scenarios where the default pixel dimension is 4096 pixels which corresponds to a 64×64 phantom when no *a priori* is applied. When *a priori* from a single projection angle are incorporated, the dimensionality is reduced, such as in Phantom 1, where the search space size decreases to 3200, representing 78.12% of the original dimensions, and in Phantom 3, where it reduces to 1600, representing 39.06% of the original size. As the number of angles increases, further reductions are observed across all phantoms. For instance, in Phantom 1, the search size decreases progressively from 3200 (1 angle) to 1349 (6 angles), representing 32.93% of the original dimensions, while in Phantom 3, it reduces to 367 (8.86%) with 6 angles. The most significant dimensionality reduction is observed in Phantom 3, attributed to its smaller and more isolated reconstruction region, which consists predominantly of empty spaces.

Therefore, as the number of projection angles increases, the *a priori* maps become progressively refined, effectively isolating valid regions of the phantom while masking non-contributing areas (see Figure 1. This refinement demonstrates the efficacy of multi-angle *a priori* in enhancing reconstruction accuracy by focusing computational efforts on the relevant regions.

5 Experiments and Results

The DFO optimizer was run with optimal settings as presented in [5] where $N = 2$, $\sigma = 1.7320508$, and $\Delta = 0.001$ for 100,000 functional evaluations (FEs) on each phantom. The dataset used for the experiments contain five phantoms of size 64^2, where phantoms 1-4 are binary reconstruction phantoms and phantom 5 is the Shepp-Logan phantom. The experiments are focused on sparse-view scenarios with 6 projection angles for reconstruction and *a priori* incorporation to simulate the extreme-few view scenario, demonstrating the role of dimensionality reduction.

5.1 Results

All experiments are simulated under the few-view scenario with only 6 projection angles. Table 2 lists the e_1 and e_2 median errors for 30 runs. This is then followed by the results of the Wilcoxon rank sum statistical analysis at a confidence level of 95% to assess the improvement of DFO-DR with different projection *a priori* which are shown in Table 3 and Table 4.

The results indicate a proportional relationship between the number of angular *a priori* and image quality. It is observed that when *a priori* are applied, the e_1 and e_2 errors are lower and decrease further as the angular *a priori* increase from two *a priori* angles as represented by DFO-DR 2 to six *a priori* angles in DFO-DR 6 which is demonstrated as the best performing reproducing method among all DFO-DR configurations and is the best overall performer among the algorithms used in this study including the toolbox algorithms when comparing e_2 scores. The incorporation of additional angular *a priori* allows for more effective masking of non-contributing regions in the reconstructed image, resulting in further dimensionality reduction. This reduction eliminates noise, particularly in peripheral and non-contributing regions, thereby enhancing reconstruction quality. The highlight of this paper is addressing the trade-off between reduced blurriness for increased noise in reconstruction reported in [5]. Figure 2 illustrates the reconstructed phantoms for all algorithms including DFO with *a priori* map applied. It is observable that there is a significant reduction in noise for phantoms with *a priori* map applied where more angular *a priori* contribute towards lower noise and thus higher image quality, therefore achieving reduction in both blurriness and noise.

The reconstruction error e_1 measures how well the predicted sinogram matches the observed data, focusing on accuracy in the projection domain. However, this does not always guarantee that the reconstructed image will be visually accurate or faithful to the original object. By contrast, reproduction error e_2 directly evaluates how closely the reconstructed image resembles the original phantom, making it a more reliable indicator of image quality in applications where clear and interpretable reconstructions are crucial.

	Phantom 1		Phantom 2		Phantom 3		Phantom 4		Phantom 5	
	e_1	e_2	e_1	e_2	e_1	e_2	e_1	e_2	e_1	e_2
FBP	881101300	425778	2552608300	396555	1572601300	396969	13681514000	341521	1179886800	326454
ART	511	216081	21532	306143	3449	239804	8068	359476	2881	289093
SART	2	214884	7	300664	0	236242	10	351830	0	287494
SIRT	0	246053	0	308809	0	243335	0	369252	0	292781
DFO-TR	20745893	46911	14819366	73059	30909058	43668	4667552	140024	5082287	113467
DFO-DR 2	48676	2850	1120890	30206	133	85	1773380	133713	194098	100533
DFO-DR 3	36489	2370	1059414	30162	1.56	4.58	10201136	131285	170572	99237
DFO-DR 6	4504	596	847241	27393	0	0	622193	129755	111108	98332

Table 2: Table representing e_1 and e_2 values for different algorithms across five phantoms in the extreme few-view scenario

Algorithm	ART	CGLS	FBP	SART	SIRT	DFO	DFO-DR 2	DFO-DR 3	DFO-DR 6
ART	NA	0	5	0	0	5	4	4	4
CGLS	5	NA	5	0	0	5	5	4	4
FBP	0	0	NA	0	0	5	2	1	1
SART	5	5	5	NA	0	5	5	4	4
SIRT	5	5	5	5	NA	5	5	4	4
DFO	0	0	0	0	0	NA	0	0	0
DFO-DR 2	1	0	3	0	0	5	NA	0	0
DFO-DR 3	1	1	4	0	0	5	4	NA	0
DFO-DR 6	1	1	4	1	1	5	5	5	NA

Table 3: Algorithm comparison based on e_1. The numbers indicate statistically significant wins for the algorithm in the left-hand column versus the algorithm in the top row.

Algorithm	ART	CGLS	FBP	SART	SIRT	DFO	DFO-DR 2	DFO-DR 3	DFO-DR 6
ART	NA	5	4	0	5	0	0	0	0
CGLS	0	NA	2	0	0	0	0	0	0
FBP	1	3	NA	1	1	0	0	0	0
SART	5	5	4	NA	5	0	0	0	0
SIRT	0	5	4	0	NA	0	0	0	0
DFO	5	5	5	5	5	NA	0	0	0
DFO-DR 2	5	5	5	5	5	5	NA	0	0
DFO-DR 3	5	5	5	5	5	5	4	NA	0
DFO-DR 6	5	5	5	5	5	5	5	5	NA

Table 4: Algorithms comparison based on e_2. The numbers indicate statistically significant wins for the algorithm in the left-hand column versus the algorithm in the top row.

The toolbox algorithms are effective at minimizing e_1, but they often produce blurred images with artifacts. Conversely, the DFO-DR configurations prioritize minimizing e_2, resulting in sharper reconstructions and better preservation of the object's internal structures and details.

Table 3 reports on the Wilcoxon statistical significance test on reconstruction error, $e1$ for the algorithms at a significance level of 0.05. The rows indicate the instances that an algorithm performed better than the algorithm in the corresponding column. It is observable that the toolbox algorithms ART, CGLS, FBP, SART and SIRT all outperform the standard DFO configuration across all 5 phantoms. DFO with three and six *a priori* masking configurations (DFO-DR3 and DFO-DR6) have shown improvement by outperforming FBP in four phantoms against FBP and all five phantoms against standard DFO configuration. However, the best performing DFO configuration, DFO-DR6 still generally underperforms in comparison to other toolbox techniques in four out of five phantoms in comparison to ART, CGLS, SART and SIRT.

Table 4 reports on the reproduction error, $e2$ Wilcoxon statistical significance test. It is observable that all DFO configurations outperform all the toolbox algorithms across all phantoms. The DFO configurations with *a priori* masking applied have shown further improvement over standard DFO across all five phantoms. DFO-DR6 emerges as the outperforming algorithm across all phantoms

and comparisons, thereby showcasing the impact on the angular *a priori* and its related masking on the reconstruction quality.

Table 5 presents the detailed $e2$ results where the cells display the median of 30 trials for each phantom where lighter shading indicates lower $e2$ and vice versa. The $e2$ results demonstrate that the presented approach consistently achieves lower reproduction error e_2 across all phantoms when compared to the toolbox algorithms. Among the toolbox methods, the highest $e2$ error is observed with CGLS for Phantoms 2, 4, and 5, while FBP exhibits the highest errors for Phantoms 1 and 3, aligning with findings reported by [5].

For Phantom 1, the introduction of just two angular *a priori* resulted in a 93% reduction in e_2 error, which was further reduced by an additional 16.85% and 75% with three and six *a priori*, respectively. The best-performing configuration, DFO-DR6, achieved 98.73% improvement in e_2 compared to the DFO configuration without *a priori* maps on phantom 1. The performance of DFO-DR6 excelled the most for Phantoms 1 and 3, where the largest reductions in reproduction error were observed. For Phantom 3, the reproduction error e_2 reached zero, indicating that the exact reconstruction of the original phantom was achieved.

In contrast, the improvements for phantoms 4 and 5 were 7.4% and 13.52% respectively which indicates limitations with reconstruction algorithms due to the more complex phantoms.

5.2 Total Variation Regularization

The *a priori* masking technique effectively removes noise and artifacts outside the object by eliminating non-contributing pixels. However, it does not improve the internal structure of the reconstructed image, where noise can still be present. To address this, Total Variation (TV) regularization was used to smooth and reduce noise inside the object while preserving important edges. TV regularization functions by encouraging the reconstruction of a more uniform image, helping to enhance fine details. However, it can fail to effective remove noise from the outer regions. By combining *a priori* masking for external noise removal with TV regularization for internal smoothing, the reconstruction process becomes more effective, in essence, utilizing two complementing methods.

Per work from [8], further refinement is performed to further enhance denoising with the *a priori* map. The best performing DFO configuration, namely DFO-DR6 is selected and total variation regularization is performed with the Shepp-Logan phantom for the 64×64 phantom to assess the impact of applying both total variation regularization and *a priori* masking on the quality and noise of the image. To finetune the adjustable parameter, μ, a range of values spanning from $[0, 1000]$ is selected, with 30 independent trials conducted for each μ value to conduct a statistical evaluation of the outcome.

Table 6 shows the effect of the μ parameter on the e_1 and e_2 error where the best μ range is between $\mu = [95, 200]$. The best statistically significant performer is found to be $\mu = 95$ with 24 significant wins out of 24.

Visual observations in Figure 3 confirm the hypothesis where the incorporation of *a priori*-mapping with total variation regularization results in much sharper reconstructions of the internal structures whereas salt-and-pepper noise has been eliminated from the external regions. Furthermore, the hybrid incorporation of *a priori* masking with the total variation regularization is shown to produce sharper reconstruction which is visually more indicative of the grey pixels present in the original phantom as compared to using TV regularization or *a priori* masking independently.

μ	(a) Error values		(b) Statistically significant cases	
	e_1	e_2	e_1	e_2
0	108777	95650	24	0
1	373924	98221	23	1
5	1403682	97100	22	2
10	2608908	96155	21	4
15	3731809	94166	20	5
20	4785380	91390	19	3
25	5702015	90640	18	6
30	6559728	88319	17	8
35	7358343	87218	16	11
40	8050741	85279	15	9
45	8670224	84284.	14	10
50	9332369	82796	13	7
55	9869655	82235	12	17
60	10357761	81661	11	12
65	10947302	80015	10	14
70	11430802	79931	9	18
75	11832489	78829	8	19
80	12282988	77939	7	16
85	12678018	77016	6	13
90	13216012	77073	5	15
95	13696451	76154	4	24
100	14131145	76164	3	23
150	18419890	74830	2	20
200	23113224	73997	1	20
1000	90728610	75997	0	22

Table 6: Fine-tuning results for μ: (a) Median error values for e_1 and e_2, (b) Statistically significant scenarios for e_1 and e_2. Darker shading represents the largest statistically significant outperformance.

6 Conclusions

This paper presents the application of a real-time prior by constructing *a priori* maps using sinogram detector values obtained from parallel projections. The study evaluates three *a priori* incorporation strategies, comparing their impact on the error metrics and the reconstruction quality. The findings demonstrate that the use of *a priori* maps and masking effectively reduces errors in both the reconstruction (e_1) and reproduction (e_2) domains. Visual results further support these observations, showing significant salt-and-pepper noise elimination. Among the tested techniques, the DFO with six angular *a priori* (DFO-DR6) emerged as the most effective, achieving the lowest errors, primarily due to enhanced dimensionality reduction that facilitated more efficient noise elimination during image masking. Furthermore, improvements in image quality were evident, with DFO-DR6, DFO-DR3, and DFO-DR2 ranking first, second, and third, respectively in terms of the lowest e_2 values across all the compared algorithms. This work builds on and optimizes

Figure 2: Visual reconstruction comparison of toolbox algorithms with all DFO configurations. It is observable that DFO configurations with more angular *a priori* result in sharper reconstruction with salt-and-pepper noise removed.

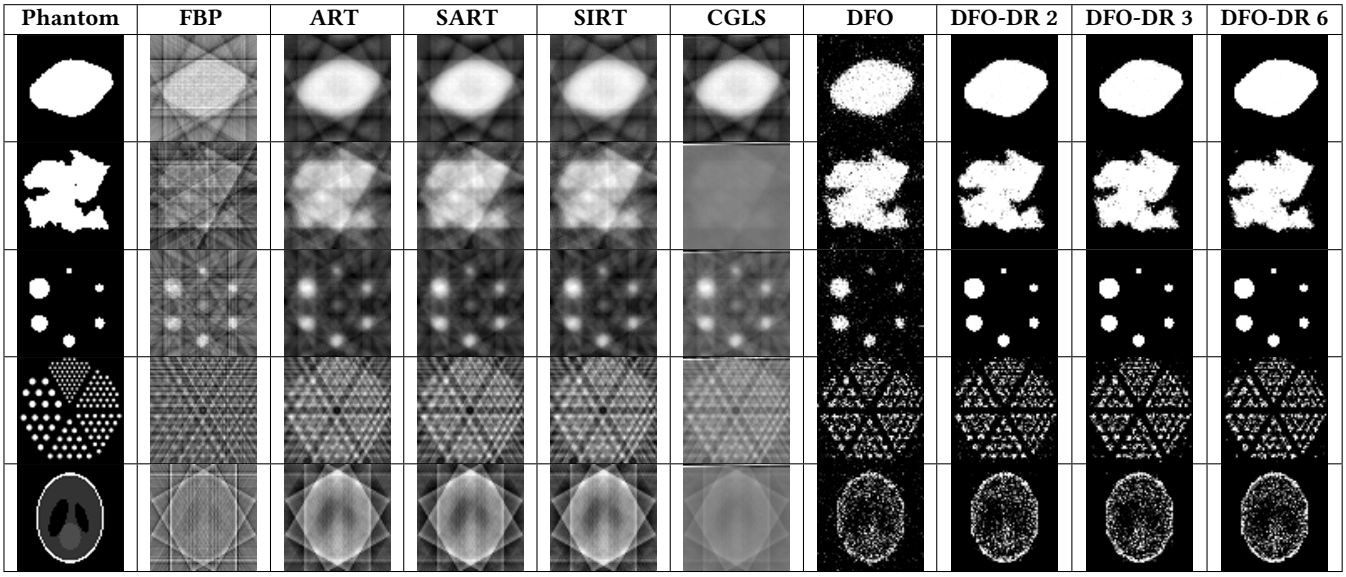

	ART	CGLS	FBP	SART	SIRT	DFO	DFO-DR 2	DFO-DR 3	DFO-DR 6
Phantom 1	215811	416802	426382	214874	246054	46911	2850	2370	596
Phantom 2	306104	481477	397097	300757	308809	73059	30206	30162	27393
Phantom 3	239967	352404	397112	236259	243334	43668	85	4	0
Phantom 4	359961	453232	341694	351839	369251	140024	133713	131285	129755
Phantom 5	289161	417457	325745	287476	292780	113467	100532	99237	98134

Table 5: Reproduction error, e_2, for each algorithm across the 5 phantoms. Darker shading represents a larger difference between reconstruction and phantoms and vice versa.

Figure 3: Shepp-Logan Phantom Observation for TV-Regularization and *a priori* Masking applied

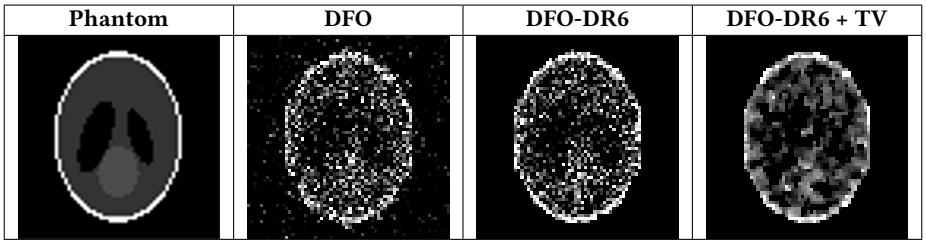

the performance of the swarm algorithms introduced in this area. Further experiments incorporating Total Variation regularization have demonstrated additional improvements in image smoothing and noise reduction, leading to a decrease in the reproduction error. Improving the effectiveness of the proposed method over the more complex phantoms is the subject of current investigation.

Future directions could include incorporating additional angles to achieve higher degrees of dimensionality reduction to further refine the reconstruction accuracy by selectively masking non-contributory regions. Additionally, integrating adaptive or data-driven *a priori* selection methods, such as learning-based approaches, could dynamically determine the optimal set of angles based on the structure of the object being reconstructed. Another promising avenue is the exploration of hybrid reconstruction strategies that combine the benefits of data-driven and model-based approaches to leverage both learned *a priori* and physical constraints.

References

[1] Bishwa Babu Acharya, Sandeep Dhakal, Aayush Bhattarai, and Nawraj Bhattarai. 2021. PID speed control of DC motor using meta-heuristic algorithms. *International Journal of Power Electronics and Drive Systems* 12, 2 (2021), 822.
[2] Mohammad Majid al-Rifaie. 2014. Dispersive flies optimisation. In *2014 Federated Conference on Computer Science and Information Systems*. IEEE, 529–538.
[3] Mohammad Majid al-Rifaie. 2021. Exploration and exploitation zones in a minimalist swarm optimiser. *Entropy* 23, 8 (2021), 977.

[4] Mohammad Majid al-Rifaie and Ahmed Aber. 2016. Dispersive Flies Optimisation and Medical Imaging. In *Recent Advances in Computational Optimization*. Springer, 183–203.

[5] Mohammad Majid al-Rifaie and Tim Blackwell. 2022. Swarm Led Tomographic Reconstruction. In *Genetic and Evolutionary Computation Conference (GECCO '22)* (2022-07-09/2022-07-13). ACM, Boston, MA, United States.

[6] Mohammad Majid al-Rifaie and Tim Blackwell. 2022. Swarm optimised few-view binary tomography. In *International Conference on the Applications of Evolutionary Computation (Part of EvoStar)* (2022-04-20/2022-04-22). EvoStar, Madrid, Spain. [Conference or Workshop Item].

[7] Mohammad Majid al-Rifaie and Tim Blackwell. 2023. Tomographic Reconstruction with Search Space Expansion. In *Proceedings of the Genetic and Evolutionary Computation Conference (GECCO '23)* (Lisbon, Portugal, 15-19 July 2023).

[8] Mohammad Majid al-Rifaie and Tim Blackwell. 2024. Tomographic Reconstruction and Regularisation with Search Space Expansion and Total Variation. arXiv:2406.01469 [cs.NE] https://arxiv.org/abs/2406.01469

[9] Mohammad Majid al-Rifaie and Marc Cavazza. 2022. Evolutionary Optimisation of Beer Organoleptic Properties: A Simulation Framework. *Foods* 11, 3 (Jan 2022), 351. doi:10.3390/foods11030351

[10] Mohammad Majid al-Rifaie, Anna Ursyn, Robert Zimmer, and Mohammad Ali Javaheri Javid. 2017. On Symmetry, Aesthetics and Quantifying Symmetrical Complexity. In *Computational Intelligence in Music, Sound, Art and Design: EvoMUSART 2017*, João Correia, Vic Ciesielski, and Antonios Liapis (Eds.). Springer International Publishing, 17–32. doi:10.1007/978-3-319-55750-2_2

[11] Haya Abdullah Alhakbani and Mohammad Majid al-Rifaie. 2017. Optimising SVM to classify imbalanced data using dispersive flies optimisation. In *2017 Federated Conference on Computer Science and Information Systems (FedCSIS)*. IEEE, 399–402.

[12] A. H. Andersen and A. C. Kak. 1984. Simultaneous algebraic reconstruction technique (SART): A superior implementation of the ART algorithm. *Ultrasonic Imaging* 6, 1 (1984), 81–94.

[13] Prashant Aparajeya, Frederic Fol Leymarie, and Mohammad Majid al-Rifaie. 2019. Swarm-Based Identification of Animation Key Points from 2D-medialness Maps. In *Computational Intelligence in Music, Sound, Art and Design*, Anikó Ekárt, Antonios Liapis, and María Luz Castro Pena (Eds.). Springer International Publishing, Cham, 69–83.

[14] Aniket Basu, Hooman Oroojeni, Georgios Samakovitis, and Mohammad Majid al-Rifaie. 2024. Three-dimensional drone cell placement: drone placement for optimal coverage. *Future Internet* 16, 11 (2024), 401.

[15] J. Mark Bishop and Mohammad Majid al-Rifaie. 2016. Autopoiesis in Creativity and Art. In *Proceedings of the 3rd International Symposium on Movement and Computing* (Thessaloniki, GA, Greece) *(MOCO '16)*. ACM, New York, NY, USA, Article 27, 6 pages. doi:10.1145/2948910.2948948

[16] Tim Blackwell. 2012. A Study of Collapse in Bare Bones Particle Swarm Optimization. *IEEE Transactions on Evolutionary Computation* 16, 3 (2012), 354–372. doi:10.1109/TEVC.2011.2136347

[17] Thorsten M. Buzug. 2011. *Computed Tomography*. Springer Berlin Heidelberg, Berlin, Heidelberg, 311–342. doi:10.1007/978-3-540-74658-4_16

[18] Zihao Cai, Zheqiang Zhong, and Bin Zhang. 2023. High-resolution restoration of solar images degraded by atmospheric turbulence effect using improved CycleGAN. *New Astronomy* (2023), 102018. doi:10.1016/j.newast.2023.102018

[19] Ling Chen, Xikai Yang, Zhishen Huang, Yong Long, and Saiprasad Ravishankar. 2023. Multi-layer clustering-based residual sparsifying transform for low-dose CT image reconstruction. *Medical Physics* 50, 10 (Oct. 2023), 6096–6117. doi:10.1002/mp.16645

[20] Wenxiang Cong and Ge Wang. 2020. X-ray Monochromatic Imaging from Single-spectrum CT via Machine. (June 2020).

[21] Marco Dorigo, Vittorio Maniezzo, and Alberto Colorni. 1996. Ant System: Optimization by a colony of cooperating agents. *IEEE Transactions on Systems, Man, and Cybernetics, Part B (Cybernetics)* 26, 1 (1996), 29–41. doi:10.1109/3477.484436

[22] Marco Dorigo, Vittorio Maniezzo, and Alberto Colorni. 1996. The ant system: Optimization by a colony of cooperating agents. *IEEE Transactions on Systems, Man, and Cybernetics, Part B (Cybernetics)* 26, 1 (1996), 29–41.

[23] Andries P. Engelbrecht. 2005. *Fundamentals of Computational Swarm Intelligence*. John Wiley Sons.

[24] Lin Fu and Bruno De Man. 2022. Deep learning tomographic reconstruction through hierarchical decomposition of domain transforms. *Visual Computing for Industry, Biomedicine, and Art* 5, 1 (Dec. 2022), 30. doi:10.1186/s42492-022-00127-y

[25] P Gilbert. 1990. Iterative methods for the three-dimensional reconstruction of an object from projections. *Journal of Geophysical Research* 95, B8 (aug 1990), 12553. doi:10.1029/JB095iB08p12553

[26] Preeti Gopal, Ritwick Chaudhry, Sharat Chandran, Imants Svalbe, and Ajit Rajwade. 2017. Tomographic Reconstruction Using Global Statistical Priors. In *2017 International Conference on Digital Image Computing: Techniques and Applications (DICTA)*. 1–8. doi:10.1109/DICTA.2017.8227496

[27] Richard Gordon, Robert Bender, and Gabor T. Herman. 1970. Algebraic reconstruction techniques (ART) for three-dimensional electron microscopy and X-ray photography. *Journal of Theoretical Biology* 29, 3 (1970), 471–481.

[28] Gabor T. Herman and Attila Kuba. 1999. *Discrete Tomography: Foundations, Algorithms, and Applications*. Birkhäuser Boston.

[29] Jiang Hsieh. 2003. *Computed Tomography: Principles, Design, Artifacts, and Recent Advances*. SPIE Press.

[30] Kyong Hwan Jin, Michael T. McCann, Emmanuel Froustey, and Michael Unser. 2017. Deep Convolutional Neural Network for Inverse Problems in Imaging. *IEEE Transactions on Image Processing* 26, 9 (Sept. 2017), 4509–4522. doi:10.1109/tip.2017.2713099

[31] Kacmarz. 1973. (0 1973).

[32] Derviş Karaboğa. 2007. A powerful and efficient algorithm for numerical function optimization: artificial bee colony (ABC) algorithm. *Journal of Global Optimization* 39, 3 (2007), 459–471. doi:10.1007/s10898-007-9149-x

[33] Davood Karimi, Pierre Deman, Rabab Ward, and Nancy Ford. 2016. A sinogram denoising algorithm for low-dose computed tomography. *BMC Medical Imaging* 16, 11 (2016). doi:10.1186/s12880-016-0112-5

[34] James Kennedy and Russell Eberhart. 1995. Particle swarm optimization. In *Proceedings of ICNN'95 - International Conference on Neural Networks*, Vol. 4. IEEE, 1942–1948.

[35] J Lacer, B M ter Haar Romeny, and M A Viergever. 1992. The use of geometric prior information in Bayesian tomographic image reconstruction: A preliminary report. Lawrence Berkeley Lab., CA (United States). https://www.osti.gov/biblio/10183584

[36] Raghavendra Mishra and Manish Bajpai. 2022. Hybrid multiagent based adaptive genetic algorithm for limited view tomography using oppositional learning. *Biomedical Signal Processing and Control* 75 (May 2022), 103610. doi:10.1016/j.bspc.2022.103610

[37] Hooman Oroojeni, Mohammad Majid al-Rifaie, and Mihalis A. Nicolaou. 2018. Deep Neuroevolution: Training Deep Neural Networks for False Alarm Detection in Intensive Care Units. In *European Association for Signal Processing (EUSIPCO) 2018*. IEEE, 1157–1161. doi:10.23919/EUSIPCO.2018.8552944

[38] Daniël M Pelt and Vincent De Andrade. 2016. Improved tomographic reconstruction of large-scale real-world data by filter optimization. *Advances in Structural and Chemical Imaging* 2, 17 (2016). doi:10.1186/s40679-016-0033-y

[39] Mariusz Pleszczynski, Adam Zielonka, and Marcin Woźniak. 2022. Application of Nature-Inspired Algorithms to Computed Tomography with Incomplete Data. *Symmetry* 14, 11 (October 2022), 2256. doi:10.3390/sym14112256 CC BY 4.0.

[40] Mariusz Pleszczyński, Adam Zielonka, Dawid Połap, Marcin Woźniak, and Jacek Mańdziuk. 2021. Polar Bear Optimization For Industrial Computed Tomography With Incomplete Data. In *2021 IEEE Congress on Evolutionary Computation (CEC)*. 681–687. doi:10.1109/CEC45853.2021.9504750

[41] S. A. Qureshi, A. U. Rehman, A. A. Mir, M. Rafique, and W. Muhammad. 2022. Simulated Annealing-Based Image Reconstruction for Patients With COVID-19 as a Model for Ultralow-Dose Computed Tomography. *Frontiers in Physiology* 12 (2022), 737233. doi:10.3389/fphys.2021.737233

[42] G. N. Ramachandran and A. V. Lakshminarayanan. 1971. Three-dimensional reconstruction from radiographs and electron micrographs: application of convolutions instead of Fourier transforms. *Proceedings of the National Academy of Sciences* 68, 9 (1971), 2236–2240.

[43] Sajib Kumar Saha, Murat Tahtali, Andrew Lambert, and Mark Pickering. 2016. Sparsity Prior Computed Tomography Reconstruction Using a Nonstandard Simultaneous X-ray Acquisition Model. *Journal Name* 47, 3 (September 2016), 251–266.e1.

[44] Sara Soltani, Misha E. Kilmer, and Per Christian Hansen. 2016. A tensor-based dictionary learning approach to tomographic image reconstruction. *BIT Numerical Mathematics* 56, 4 (February 2016), 1425–1454.

[45] Wim Van Aarle, Willem Jan Palenstijn, Jeroen Cant, Eline Janssens, Folkert Bleichrodt, Andrei Dabravolski, Jan De Beenhouwer, K Joost Batenburg, and Jan Sijbers. 2016. Fast and flexible X-ray tomography using the ASTRA toolbox. *Optics express* 24, 22 (2016), 25129–25147.

[46] Gengsheng L. Zeng. 2010. *Medical Image Reconstruction: A Conceptual Tutorial*. Springer.

[47] Jiayong Zhang, Wah-Keat Lee, and Mingyuan Ge. 2022. Sub-10 second fly-scan nano-tomography using machine learning. *Communications Materials* 3, 1 (November 2022), 91. doi:10.1038/s43246-022-00313-8 License: CC BY 4.0.